Simultaneous observations of polar mesosphere winter echoes and cosmic noise absorptions in a common volume by the PANSY radar (69.0°S, 39.6°E)

T. Nishiyama[1,2], K. Sato[3], T. Nakamura[1,2], M. Tsutsumi[1,2], T. Sato[4], Y. Tanaka[1,2], K. Nishimura[1,2], Y. Tomikawa[1,2], and M. Kohma[3]

[1]National Institute of Polar Research, Tachikawa, Tokyo, Japan.
[2]SOKENDAI (The Graduate University for Advanced Studies), Tachikawa, Tokyo, Japan.
[3]Department of Earth and Planetary Science, The University of Tokyo, Japan.
[4]Department of Communications and Computer Engineering, Kyoto University, Japan.

Key Points:

- The PANSY radar observed simultaneous PMWE and CNA.
- PMWE below (above) 70 km intensified (decayed) with large CNA.
- The PMWE decay can be caused by small *Sc* or an increase in electron diffusivity due to high electron density.

Corresponding author: Takanori Nishiyama, nishiyama.takanori@nipr.ac.jp

Abstract

This study focuses on the one-to-one relationship between the morphology of polar mesosphere winter echo (PMWE) and cosmic noise absorption (CNA) as determined by measurements made with a single atmospheric radar, the Program of the Antarctic Syowa mesosphere-stratosphere-troposphere/incoherent scatter (PANSY) radar. CNA was calculated using the noise level in radar signal data collected during May, 2013, including data of a Solar Proton Event (SPE) on 23 May. Using PMWE and CNA data in a common volume, their temporal variations and relation were examined in detail. PMWE altitude was clearly anti-correlated with CNA magnitude in a statistical sense: when a large CNA exceeding 0.50 dB took place, PMWE seemed to concentrate around 65 km and disappear above 70 km. The electron density behind the PMWE was estimated by using the Ionospheric Model for the Auroral Zone (IMAZ) for the SPE. PMWE occurrence roughly coincided with a high electron density in the model, except that no PMWE was observed above 70 km at 0730 UT despite the electron density being higher than 10^8 m^{-3}. Additionally, the estimated radar volume reflectivity with a normal or small value of the Schmidt number *Sc* is qualitatively consistent with the observed PMWE. Although weak turbulent energy dissipation rate can also play a dominant role in the observed PMWE decay, a plausible mechanism was small *Sc* or reduction of *Sc* that is equal to an increase in electron diffusivity resulting from an unusually high electron density, which significantly reduced radar volume reflectivity above 70 km.

1 Introduction

Polar mesosphere winter echo, PMWE, is a coherent echo observed by both mesosphere-stratosphere-troposphere (MST) radars and incoherent scatter (IS) radars in the VHF range, and it was discovered almost four decades ago [*Czechowsky et al.*, 1979; *Ecklund and Balsley*, 1981]. As indicated by the name, it is a weak radar echo that is commonly observed in the polar regions during non-summer periods. Recent studies on PMWE have reported its characteristics as follows [*Zeller et al.*, 2006; *Kirkwood*, 2007; *Strelnikova and Rapp*, 2013; *Latteck and Strelnikova*, 2015]. PMWE is typically scattered and observed from 55 km to 85 km. The most of the echo is concentrated at altitudes near 70 km. With regard to the morphology, it usually appears as multiple echo layers with vertical intervals of several km. The echo power is a few orders of magnitude weaker than that of polar mesosphere summer echo (PMSE), which is closely related to ice particles in the coldest mesopause region [*Cho and Röttger*, 1997; *Rapp and Lübken*, 2004]. The daily occurrence rate of PMWE is high (up to 30%) around local noon. On the other hand, nighttime PMWE needs strong ionization in the upper mesosphere, e.g., due to geomagnetic disturbances.

PMWE is basically believed to result from Bragg scattering by irregularities in the refractive index, which is almost solely defined by electron density at PMWE altitudes, that arise from neutral turbulence with half-wavelength-scale structures. [*Czechowsky et al.*, 1989; *Brattli et al.*, 2006; *Lübken et al.*, 2007]. Note that this process is not necessarily limited to the polar mesosphere and is common in mesospheric echoes in mid-latitude and equatorial regions [*Czechowsky et al.*, 1979; *Tsuda et al.*, 1990; *Kubo et al.*, 1997; *Zeller et al.*, 2006; *Lehmacher et al.*, 2009; *Selvaraj et al.*, 2014]. Neutral turbulence is likely to be generated by gravity wave breaking [*Lübken et al.*, 2006; *Rapp et al.*, 2011]. It is obvious that free electrons, as well as neutral turbulence, in the mesosphere are important for mesospheric coherent echoes in the VHF range. However, direct comparisons of PMWE with background electron density have been rather limited [*Belova et al.*, 2005; *Kirkwood*, 2007; *Lübken et al.*, 2006, 2007].

Either infrasound waves propagating into the mesosphere [*Kirkwood et al.*, 2006a,b] or dust particles originating from meteors [*Rosinski and Snow*, 1961; *Hunten et al.*, 1980] have been thought to contribute to PMWE instead of neutral turbulence. Recently, radar observations of PMWE, coordinated with artificial heating experiments on plasma in *D* region, demonstrated the presence of dust particles with radii of a few nm through overshoot effects in PMWE [*Kavanagh et al.*, 2006; *Havnes and Kassa*, 2009]. Dust particles are known to play a dominant role in the electron loss process at PMWE altitudes, as electrons attach themselves to the dust [*Havnes et al.*, 2011; *Friedrich et al.*, 2012].

Nishiyama et al. [2015] reported monthly averaged PMWE morphology and its seasonal variability from March to September in 2013 by using the Program of the Antarctic Syowa mesosphere-stratosphere-troposphere/incoherent scatter (PANSY) radar. Their results demonstrated that PMWE structure in height and time sections was governed on a monthly basis by photochemical reactions. In addition, rapid intensifications of PMWE associated with Solar Proton Events (SPEs), magnetic storms, and substorms were frequently identified on a daily basis. Since PMWE structure in height and time sections is directly modulated by *D* region ionization due to energetic particle precipitations (EPP) and the resultant ion chemistry [*Kirkwood et al.*, 2002; *Kero et al.*, 2008], short-time variations in PMWE morphology should be discussed in relation to local ionospheric disturbances.

Cosmic noise absorption (CNA), which is a proxy of the height-integrated electron column density in *D* region, has been compared with PMWE for a long time [*Ecklund and Balsley*, 1981; *Czechowsky et al.*, 1989; *Kirkwood et al.*, 2002]. PMWE and global geomagnetic indices such as *Kp* and *Ap* have also been compared in the context of the long-term trend of PMWE occurrences [*Zeller et al.*, 2006; *Latteck and Strelnikova*, 2015]. However, CNA is considered more suitable than geomagnetic indices for making a comparison with detailed PMWE morphology since it is a measurement of local ionospheric disturbances. However, two problems remain. One is that detailed surveys of the one-to-one relation between PMWE morphology and CNA are much fewer than those of PMSE [*Morris et al.*, 2005] and coherent echoes from *E* region [*Makarevitch and Honary*, 2005]. The other is that a single-beam riometer does not measure absorptions in the same volume as radar echoes by MST/IS radar since a riometer covers a wide area of the ionosphere with its wide beam.

In this study, we present simultaneous PMWE and CNA observations made in May 2013 by the PANSY radar. The PMWE and CNA data are originated from the same dataset of the PANSY radar in a similar way as in *Kirkwood et al.* [2015]. This is the first study focusing on the one-to-one relationship between PMWE morphology and CNA in a common volume. In section 2, a brief description of the PANSY radar and a detailed explanation of our method for estimating CNA are presented. Section 3 describes the altitude variability of PMWE with respect to CNA in a statistical sense. Additionally, it describes the background electron density corresponding to the observed PMWE as determined by an empirical electron density model. The obtained results and theoretical radar volume reflectivity are discussed in section 4, and the key findings of this study are summarized in section 5.

2 Instrumentation and analysis methods

The PANSY radar is a 47-MHz VHF radar at Syowa Station in the Antarctic (69.0°S, 39.6°E) [*Sato et al.*, 2014, 2017]. In May 2013, continuous observations were conducted with a total antenna aperture of 3,900 m^2 (18,000 m^2 for the full system) and peak transmitting power of 113 kW (520 kW for the full system). Five beams in the directions of local zenith, geographic north, east, south, and west with a zenith angle of 10° were formed. The range of measurement was from 60.0 to 97.7 km with a range resolution of 600 m. The coherent integration time was 12.8 msec, and line-of-sight Doppler velocities were measured to a maximum of ± 24.9 m s^{-1}. One data sequence in the range and Doppler frequency domain was obtained every 4 minutes. More detailed radar parameters are shown in Table 1. For the dataset used in this study, it is difficult to derive absolute radar volume reflectivity because antenna arrangement was complicated for avoiding deep snow in the winter.

Figure 1 shows diurnal variations in PMWE (signal to noise ratio, SNR, in dB) and background noise in the five directions on 23 May 2013. From 07 to 09 UT, strong PMWE was observed below 70 km in all five directions. Descending multiple layers of PMWE with relatively weaker echo power were also observed until 13 UT. The noise was estimated using the statistical method reported in *Sato et al.* [1989] and recorded on a realtime basis. Time variations in the noise are thought to be mainly due to those in cosmic noise power (CNP) as a function of Greenwich mean sidereal time (GMST). They were sometimes contaminated by interferences, as can be seen around 04 UT. Note that the temporal variations in the noise in the each of the directions in Figure 1f have been subtracted from the backscattered echo power in Figure 1a-e.

We tried to estimate CNA by using the CNP data measured by the PANSY radar in May 2013. Our analysis method was basically the same as that for riometers and applied as follows [*Krishnaswamy et al.*, 1985 and references therein]: all CNP data were reordered by GMST and then CNP was averaged using a bin with a time width of 15 minutes. In this process, we excluded the contaminated CNP and only used CNP that was measured during ionospherically quiet times when AE index was less than 100 nT. Representative CNP values under the quiet condition were determined based on percentile in each time bin. We determined through trial and error that CNP in the 90th percentile was a representative value. Finally, a quiet day curve (QDC) was obtained from a cubic polynominal interpolation of the representative CNP values as presented in Figure 2a. Figure 2b is a histogram of the obtained CNA in all five directions in May 2013. Except for its slightly longer tail at larger CNA, the distribution seems to have a gaussian shape with a mode value of 0.110 dB. Note that CNA values less than 0 dB, which are not reliable, accounts for only 12% of the total number of obtained CNAs.

3 Results

We compared the estimated CNA with other measurements at Syowa in order to confirm that ionizations in D region actually took place. Figure 3 is an overview of the influence of EPP on the ionosphere for several days after the 22 May SPE that was detected on 23 May at Syowa Station. Figure 3a shows geomagnetic field variations (H, D, Z components) observed at Syowa, which are a proxy for the ionospheric disturbances localized around Syowa. Time variations in field-aligned energetic proton flux (> 6.9 MeV), which is responsible for ionizations below 80 km [*Turunen et al.*, 2009], observed by NOAA/Polar Orbiting Environmental Satellites close to Syowa are presented in Figure 3b. Enhancements of field-aligned energetic protons that were triggered by the SPE were identified at 05 UT on 23 May.

A MF radar is also located in Syowa and continuously operating in the frequency of 2.4 MHz. Its observation shown in Figure 3c demonstrates that isolated lower mesosphere echoes (ILME) occurred at the same time as the increase in the energetic proton flux, which also implies strong ionizations in the lower mesosphere [*Hall et al.*, 2006]. Figure 3d is a height-time section of backscattered echo power observed by the PANSY radar. A sudden enhancement of PMWE below 70 km and ILME were almost simultaneously observed by these two radars. The probed volume of the PANSY radar is narrower than that of MF radar because incident angles of MF radar echo range up to 25 degrees [*Tsutsumi and Aso*, 2005]. In Figure 3e, black and red lines indicate temporal variations in QDC and CNP in the zenith direction, respectively. The many spikes seen in the CNP are likely due to contamination. The running-averaged variations for about 12 minutes in the CNA along the five beam directions are presented in Figure 3f. The peak values of CNA were about 1.0 dB in all five directions and were accompanied by a sudden enhancement in PMWE, which indicates that both intensifications of CNA and PMWE were caused by ionization in a common volume. The subsequent substorms after 25 May seems to cause intermittent CNA for a few days. Note that the substorm-related CNA (as represented by the black arrows) that took place on the dayside is likely due to EPP just after the substorms (as highlighted in semi-transparent gray). Observational results of both the radars and estimated CNA on 29 May imply a recovery of the lower ionosphere from disturbed conditions. The temporal variations in the estimated CNA are consistent with other observations as shown in Figure 3. Therefore, it can be concluded that our analysis method successfully identified CNA events, which were related to EPP triggered by the 23 May SPE and the subsequent substorm.

Next we focused on PMWE variabilities with respect to CNA in order to investigate differences in PMWE characteristics, especially altitude, between the ionospherically quiet and disturbed periods. The estimated CNA around 23 May, 2013 had the largest amplitude during the period presented by our previous work [*Nishiyama et al.*, 2015]. So we used the dataset in this month and carried out more detailed analysis. The weighted mean center altitude (WMCA) of PMWE, h_c, is defined by the following equation:

$$h_c(t) = \frac{\sum_{i=0}^{N-1} P(t, h_i) \cdot h_i}{\sum_{i=0}^{N-1} P(t, h_i)} \qquad (1)$$

Here, t is time, h is altitude, and P is SNR of PMWE as functions of time and altitude in units of dB. We used a logarithmic scale because the probability distribution of PMWE SNR approaches a gaussian more closely on it than on a linear scale. We produced PMWE SNR data with time and range resolutions of 15 min and 600 m, respectively, by using the analysis method presented in *Nishiyama et al.* [2015]. Note that all PMWE SNR is defined as deviations from 6 dB, which was the lowest SNR of PMWE, so that all $P(t, h_i)$ must be greater than 0 dB.

Figure 4a is a scatter plot of CNA and WMCA of PMWE. CNA was averaged over 15 min for this plot. Red and blue crosses represent data sampled during the ionospherically disturbed period and quiet periods, respectively. The results demonstrate that the WMCA of PMWE became significantly lower than 70 km when CNA was greater than 0.6 dB. Figures 4b and 4c are two-dimensional number distributions as functions of CNA and WMCA of PMWE during the disturbed period and quiet periods, respectively. Horizontal and vertical bin widths are 0.05 dB and 1.0 km, respectively. Though the WMCA of PMWE was widely distributed from 60 to 80 km with no dependence on CNA during the quiet period, CNA and WMCA of PMWE during the disturbed period showed a good negative correlation. These results imply that electron density enhancement due to EPPs allows us to observe PMWE at lower altitudes more frequently than at higher altitudes. However, the most of the PMWE occurred at 70-80 km altitudes without CNA, which indicates that electron density enhancements due to EPPs are not necessarily required for PMWE. In addition, it is noted that data plotted above 80 km were contaminated due to meteor echoes in the three figures. The method in *Nishiyama et al*. [2015] seems to be not perfect yet. However, separation between PMWE and meteor echo in the figures seemed to be successfully done.

Figures 5a and 5b are number and averaged SNR distributions of PMWE, respectively, as functions of CNA and altitude. Horizontal and vertical bin widths are 0.1 dB and 2.4 km, respectively. Bins with data sample numbers less than 10 are not plotted in the two figures. Again, most of the PMWE was observed when CNA was less than 0.5 dB, as shown in Figure 5a. It is clear that PMWE was less frequently observed above 70 km when CNA became larger than about 0.6 dB. Figure 5b demonstrates that the PMWE profiles changed with respect to CNA. As CNA increased PMWE was observed in narrower altitude ranges and the peak shifted to lower altitudes.

Figure 5c shows PMWE profiles with variances and their dependence on CNA in more detail. Error bars plotted with the profiles indicate a 90% confidence interval. For weak CNA cases (0.10-0.30 dB), PMWE was observed in a wide altitude range from 60 to 80 km with small variances. The profiles had no well-defined peaks, but one peak seemed to be around 75 km. Data for altitudes higher than around 85 km were due to meteor echoes, not PMWE. For strong CNA cases (0.70-0.90 dB and 0.90-1.10 dB), although the variances were larger than in the weak CNA cases, well-defined peaks appeared around 65 km. Moreover, PMWE drastically decayed above 65 km when CNA ranged from 0.90 to 1.10 dB. In particular, the most of PMWE disappeared above 70 km in a statistical sense. These results are consistent with the finding that the WMCA of PMWE had a strong negative correlation to CNA.

Since electron density plays a dominant role in PMWE variations on a short time scale, we calculated electron density profiles by using Ionospheric Model for the Auroral Zone (IMAZ) [*McKinnell and Friedrich*, 2007]. IMAZ provides a more reliable electron density profile with an optional input parameter of CNA for 27.6 MHz. Therefore, we also calculated the CNA corresponding to 27.6 MHz (The details are in the Appendix). The ratio of CNAs at different frequencies of ω_0 and ω_1 is:

$$\frac{C(\omega_0)}{C(\omega_1)} = \frac{\omega_1^2 + \nu_e^2}{\omega_0^2 + \nu_e^2} \tag{2}$$

Here, $C(\omega)$ is the CNA value as a function of frequency, and ν_e is the collision frequency between electrons and neutrals. (The height dependence of the ratio is shown in Figure A1 of the Appendix.)

Figures 6a and 6b plot the IMAZ-calculated electron density in time-height sections on 23 May (disturbed) and on 29 May (quiet), respectively. The input parameters for the calculation were sun spot number, *F10.7* index, 3-hour averaged *Ap* index, and CNA at 27.6 MHz (See the Appendix for details). Note that the data gap in Figure 6a was caused by estimated negative CNA values. The IMAZ-calculated electron density showed a significant difference between 23 May and 29 May. In particular, near 60 km, which is minimum sampling range in this experimental setup, the electron density was estimated to be larger than 10^9 m^{-3} around 07 UT on 23 May. This value is more than 10 times as large as that during the quiet period, which implies that strong ionizations corresponding to the observed CNA enhancements also took place in the IMAZ calculation.

Figures 6c and 6d are expanded contour plots of the data as in 6a and 6b but between 05 and 15 UT and from 60 to 80 km on 23 May and on 29 May, respectively. Thirty-minute averaged PMWE SNR is plotted as red contour lines from 6 to 26 dB in a 10-dB interval. Around 07 UT on 23 May, when the increase in energetic field-aligned protons and the sudden enhancement of PMWE around 60 km were simultaneously observed, the IMAZ-calculated electron density increased (10^9 - 10^{10} m^{-3}) in a wide altitude range from 60 to 80 km. Since it was reported that electron density behind PMWE below 70 km, as measured by a rocket, was larger than 10^9 m^{-3} [*Lübken et al.*, 2006], the strong PMWE of about 10 dB near 65 km on 23 May can be explained by the electron density increase seen in the IMAZ calculation. However, no PMWE was observed from 70 to 80 km even though the IMAZ calculation indicates that the electron density is extremely high ($\sim 10^{10}$ m^{-3}) in the same altitude range. Later, we will discuss the PMWE decay above 70 km in detail.

In addition, multiple layers of weak PMWE (> 6 dB) were observed after 08 UT even in the region of relatively low electron density less than 10^9 m^{-3} below 70 km. These discrepancies probably result from that IMAZ is not history-dependent model and it does not take account into vertical and horizontal transportation and/or the time evolution of the electron density. With regard to the results on 29 May, the calculated low electron density ($< 10^9$ m^{-3}) below 80 km is consistent with the finding that no significant PMWE was observed. On the basis of the calculation for the two dates, we concluded that the IMAZ calculation seems to agree roughly with the time and altitude variations in the observed PMWE.

4 Discussion

Our results clearly demonstrated that the WMCA of PMWE became lower when strong CNA took place, which has been never reported before. They can be explained as being due to strong ionizations in the lower PMWE altitudes (below 70 km) associated with EPP. However, above 70 km, PMWE was less frequently observed during ionospherically disturbed periods than during quiet periods as shown in Figure 5. This absence of PMWE is considered to be not instrumental effects such as Faraday rotation due to strong ionization, because circularly polarized antennas are used in the PANSY radar system [*Chau et al.*, 2013].

For further investigation on that characteristic, we calculated a radar volume reflectivity as a function of altitude and its variability with respect to electron density profiles. The radar volume reflectivity for a Driscoll and Kennedy (D&K) spectrum [*Driscoll and Kennedy*, 1985], $\eta^{D\&K}$, is described as

$$\eta^{D\&K}(k) = 8\pi^2 \cdot k^4 \cdot Q^{9/2} A \chi_n \varepsilon^{-1/3} \eta_{Kol}^{11/3} \cdot D(y) \tag{3}$$

where, k is wave number, $Q = 2$, $A = 0.033 \cdot a^2$, $a^2 = 1.74$, ε is turbulent energy dissipation rate, $\eta_{Kol}(= (\nu^3/\varepsilon)^{1/4})$ is Kolmogorov microscale, ν is kinematic viscosity as a function of altitudes, and χ_n is variance dissipation rate. It should be noted that χ_n depends on various background parameters and can be written as $\chi_n = f(\varepsilon, N_e, dN_e/dz, Ri, Pr, \omega_B, H_N)$, by using the Richardson number, Ri, the Prandtle number, Pr, Brunt-Väisälä frequency, ω_B, and scale height, H_N. These parameters in this study were set to be the same values as in *Lübken* [2014]. $D(y)$ and y are expressed as below.

$$D(y) = (y^{-11/3} + y^{-3}) \cdot \exp\left\{-A_{3\vartheta}\left(\frac{3}{2}y^{4/3} + y^2\right)\right\} \tag{4}$$

$$y = Q^{3/2} \cdot \eta_{Kol} \cdot k \tag{5}$$

where, $A_{3\vartheta} = \frac{\alpha}{Q^2 \cdot Sc}$, $\alpha = 0.83$, and Sc is the Schmidt number, which is the ratio of kinematic viscosity to electron diffusivity.

The important parameters in the above calculation were determined as follows: ε = 0.10 W/kg corresponding to a moderate value [*Becker et al.*, 2004; *Lübken et al.*, 2006]; Sc = 1.0, which means no significant effects due to aerosols [*Kelley et al.*, 1987; *Lübken*, 2014]. Note that both ε and Sc are assumed to be constants for altitudes. The method of estimating the volume reflectivity was basically the same as that in *Lübken* [2014], but the electron density and vertical gradient of the electron density were calculated by IMAZ, which is believed to be more suitable than the international reference ionosphere (IRI) for the geomagnetic high latitude region and ionospherically disturbed periods. Additionally, we used the parameters that depended on altitude, solar activity, and geomagnetic activity: kinematic viscosity through MSISE-90 temperature. ν was calculated using Sutherland's formula as a function of the temperature and density deduced from MSISE-90 [*Hedin*, 1991].

Figure 7a shows electron density profiles at 0730 UT on 23 May (disturbed) and 29 May (quiet) as calculated by IMAZ. Dashed lines indicate the root mean square errors of electron density in the model. As well as the absolute electron number density, the vertical gradient was also changed drastically between the two dates. For example, the density profile on 23 May has a much steeper vertical gradient below 70 km.

Variabilities of the radar volume reflectivity for 3-m-scale turbulent structures on the two dates are shown in Figure 7b. The estimated volume reflectivity on 29 May (indicated by the black solid line) is not well-defined except for a positive peak at an altitude of around 65 km. Considering the peak transmitting power and the antenna area of the PANSY radar at that time, the threshold of volume reflectivity for PMWE was likely to be 2.0×10^{-17} m^{-1}, which is slightly lower than that of the ALWIN radar but higher than that of the MAARSY radar [*Latteck and Strelnikova*, 2015]. Note that the peak in radar reflectivity was much less than the threshold and is therefore it is consistent with our finding that no significant PMWE was observed at 0730 UT on 29 May (Figure 3d).

The volume reflectivity at 0730 UT on 23 May (red solid line) shows substantial increases for all altitudes. The difference is typically 3 ~ 4 orders of magnitude. Below 65 km, the reflectivity on 23 May became larger at lower altitudes, and the peak altitude was also vertically shifted to lower altitudes. This change in the reflectivity matches the enhancement in PMWE near 65 km at 0730 UT (Figure 6c). On the other hand, the reflectivity near 70 km on 23 May was estimated to be large enough to be observed by the PANSY radar at that time, which does not support our finding that no PMWE was observed above 70 km.

Next, we tried modifying the two parameters in the calculation, i.e., the Schmidt number and turbulent energy dissipation rate, independently so that the radar volume reflectivity profile approaches the observed one more closely. Figure 7c and 7d are radar volume reflectivities at 0730 UT on 23 May in the same format as Figure 7b but with modifications of the Schmidt number and turbulent energy dissipation rate, respectively. These results demonstrate that radar volume reflectivity decreases in particular above near 70 km drastically if the Schmidt number or turbulent energy dissipation rate becomes small. Among the calculated profiles, either one with $Sc = 0.5$ (and $\varepsilon = 0.10$ W/kg) or $\varepsilon = 0.05$ W/kg (and $Sc = 1.0$) is qualitatively consistent with the observation that PMWE was not detected above 70 km during large CNA periods.

Anti correlations between mesospheric coherent echoes in the VHF range and the background electron density have already been reported in a previous PMSE study [*Rapp et al.*, 2002; *Barabash et al.*, 2004]. *Rapp et al.* [2002] found that PMSE was observed less frequently at 87 km when electron number densities exceeded $\sim 7 \times 10^{10}$ m^{-3}. This result was interpreted as being due to electron-dust particle interactions that caused charge saturation of aerosol particles and an increase in electron diffusivity ($\propto 1/Sc$), thereby leading to a reduction in radar volume reflectivity [*Cho et al.*, 1992]. In addition, the reflectivity increases with increasing electron density only when the density is much less than that of charged dust [*Kirkwood et al.*, 2015]. Accordingly, the PMWE decay above 70 km can be explained by small Sc or reduction of Sc that is equal to an increase in electron diffusivity resulting from unusually high electron density. This is consistent with the model calculation shown in Figure 7c.

On the basis of our results for 23 May (Figure 6c), the threshold of electron density for PMWE decay above 70 km is estimated to be about 8×10^9 m^{-3}, which is an order of magnitude lower than that for PMSE decay at 87 km. This would be because dust particles in the mesosphere, which are known as scavengers of free electrons [*Friedrich et al.*, 2012], change in number density and peak altitude between polar winter and polar summer [*Megner et al*, 2008]. Since it is suggested that PMWE characteristics change dramatically at the transition height near 72 km [*Nishiyama et al.*, 2015], we have to re-consinder the effect of electron diffusivity on the scattering process and its relation to dust particles in PMWE layer.

Meanwhile, we cannot exclude a possibility that the observed PMWE decay above 70 km is caused by small turbulent energy dissipation rate as shown in Figure 7d. However, the decay of PMWE is more likely related to local plasma conditions directly from the point of view that it has clear CNA dependence. Since the role of turbulence around the mesopause region is also important in generating mesospheric echoes, precise radar measurements of turbulent energy dissipation rate behind PMWE layer is needed. Unfortunately, the dataset presented in this study is hard to discuss quantitatively about turbulent energy dissipation rate because the PANSY radar was operating in a quarter system at that time. Accurate measurement of this important parameter allows us to estimate the Schmidt number more precisely without any assumptions.

An understanding of the behavior of free electrons as scatterers, which includes interactions with dust particles and responses to EPP, is crucial to clarifying the radio scattering process in the VHF range. Although further investigation into such behavior is beyond the scope of this study, it should be addressed by in-situ measurements and by gaining an understanding of the ion-chemical process by taking into account dust particles, especially for ionospherically disturbed periods in a more recent study [*Baumann et al.*, 2015, 2016].

5 Conclusions

We presented a detailed study focusing on the one-to-one relationship between PMWE morphology and CNA in a common volume as measured by the PANSY radar, a single MST radar, for the first time. Our new data analysis method allowed us to estimate reasonable CNA values during the SPE on 23 May. Temporal variations in these values during May 2013 and their relation were discussed in detail.

The main results are as follows.

1. The WMCA of PMWE was clearly anti-correlated to the CNA magnitude in a statistical sense: When a large CNA exceeding 0.50 dB for the PANSY radar frequency took place, the PMWE above 70 km seemed to rapidly decay.

2. The IMAZ model provides electron density profiles for the large CNA event on 23 May. The model indicates that the electron density from 60 to 80 km is higher than a value of 10^8 m^{-3}, which is enough for PMWE generation. Except for the PMWE above 70 km at 0730 UT (CNA exceeded ~ 1.0 dB), the occurrence of PMWE and high electron density in the model coincide for the most part.

3. We estimated the radar volume reflectivity on the basis of the electron density deduced from IMAZ with CNA, MSISE-90 temperature, and typical parameters used in the preceding study. As a result, the estimated volume reflectivity with normal or small *Sc* is qualitatively consistent with the observed PMWE decay above near 70 km on 23 May. Meanwhile, we cannot exclude a possibility that weak turbulent energy dissipation rate play a dominant role in the observed PMWE decay above 70 km.

4. This PMWE decay with strong CNA can be explained by small *Sc* or reduction of *Sc* that is equal to an increase in electron diffusivity resulting from an unusually high electron density. Further investigations are needed into the behavior of free electrons as scatterers including interactions with dust particles and responses to EPP.

A: Conversion of CNA between different frequencies

The absorption coefficient, K, can be determined on the basis of the Appleton-Hartree equation as follows:

$$K(\omega) = \frac{e^2}{2\epsilon_0 m_e c\mu} \cdot \frac{N_e \nu_e}{(\omega^2 + \nu_e^2)} \tag{A.1}$$

Here, ω is radio frequency, e is elementary charge, ϵ_0 is permittivity in vacuum, m_e is mass of the electron, c is speed of light, μ is the real part of the refractive index for radio waves, and N_e is electron density. ν_e can be written as a function of pressure, p, in units of hPa, [*Gregory and Manson*, 1967]:

$$\nu_e = (6.4 \pm 0.4) \times 10^7 \cdot p \tag{A.2}$$

We calculated the temperature (Figure A1a) by using MSISE-90 in this study [*Hedin*, 1991] and subsequently obtained the pressure. The collision frequency and absorption coefficients at 47.0 MHz and 27.6 MHz are shown in Figure A1b and c. The ratio of CNAs at different frequencies of ω_0 and ω_1 is:

$$\frac{C(\omega_0)}{C(\omega_1)} = \frac{K(\omega_0)}{K(\omega_1)} = \frac{\omega_1^2 + \nu_e^2}{\omega_0^2 + \nu_e^2} \tag{A.3}$$

Note that the ratio is a constant, as shown in Figure A1d, if the absorption takes place mainly above 60 km. Using this relationship, we can obtain CNA for 27.6 MHz. Figure A2 is an overview of the temporal variations in the IMAZ input parameters, i.e., sun spot number, *F10.7* index, 3-hour averaged *Ap* index, and CNA for the two radio frequencies from 22 May to 29 May. CNA for 27.6 MHz, which is indicated by the red line in Figure A2d, was obtained by simply multiplying that for 47.0 MHz by about 2.9.

Acknowledgments

This study was supported by Grants-in-Aid for Scientific Research (A) 25247075 and (B) 24340121 of the Ministry of Education, Culture, Sports and Technology (MEXT), Japan, KP-2 and KP-301 projects of National Institute of Polar Research. PANSY is a multi-institutional project with a core of the University of Tokyo and National Institute of Polar Research. The observation data is available at the project's website, pansy.eps.s.u-tokyo.ac.jp. The provisional *AE* data were provided by the World Data Center for Geomagnetism, Kyoto. Information on SPE is available at the following address: ftp://ftp.swpc.noaa.gov/pub/indices/SPE.txt. Magnetic field data were provided by National Institute of Polar Research, Japan. The distribution of the magnetic field data has been partly supported by the IUGONET (Inter-university Upper atmosphere Global Observation NETwork) project (http://www.iugonet.org/) funded by the MEXT, Japan. Proton flux data from the Medium Energy Proton Electron Detector instrument on board low-altitude NOAA/Polar Orbiting Environmental Satellites is available at http://satdat.ngdc.noaa.gov/sem/poes/data/processed/swpc/uncorrected/avg/cdf/. Backscatter echo power data obtained from MF radar at Syowa was provided by Dr. M. Tsutsumi (tutumi@nipr.ac.jp). The Fortran source code of Ionospheric Model for the Auroral Zone (IMAZ) can be found at http://spdf.gsfc.nasa.gov/pub/models/iri/iri2007/IMAZ/. T. Nishiyama appreciates the technical supports in running IMAZ from Prof. D. Bilitza and Prof. S. Watanabe. All parameters for running IMAZ, except for CNA, are available at the following address: ftp://ftp.ngdc.noaa.gov/STP/GEOMAGNETIC_DATA/INDICES/KP_AP/. The production of this paper was supported by an NIPR publication subsidy.

References

Barabash, V., S. Kirkwood, A. Feofilov, and A. Kutepov (2004), Polar mesosphere summer echoes during the July 2000 solar proton event, *Ann. Geophys.*, *22*, 759-771.

Baumann, C., M. Rapp, M. Anttila, A. Kero, and P. T. Verronen (2015), Effects of meteoric smoke particles on the D region ion chemistry, *J. Geophys. Res. Space Physics*, *120*, doi:10.1002/2015JA021927.

Baumann, C., M. Rapp, and A. Kero (2016), Secondary electron emission from meteoric smoke particles inside the polar ionosphere, *Ann. Geophys.*, *34*, 573-580, doi:10.5194/angeo-34-573-2016.

Becker, E., A. Müllemann, F.-J. Lübken, H. Körnich, P. Hoffmann, and M. Rapp (2004), High Rossby-wave activity in Austral winter 2002: Modulation of the general circulation of the MLT during the MaCWAVE/MIDAS northern summer program, *Geophys. Res. Lett.*, *31*, doi:10.1029/2004GL019615, 2004.

Belova, E., S. Kirkwood, J. Ekeberg, A. Osepian, I. Häggström, H. Nilsson, and M. Rietveld (2005), The dynamical background of polar mesosphere winter echoes from simultaneous EISCAT and ESRAD observations, *Ann. Geophys.*, *23*, 1239-1247.

Brattli, A., T. A. Blix, Ö. Lie-Svendsen, U.-P. Hoppe, F. J. Lübken, M. Rapp, W. Singer, and M. Friedrich (2006), Rocket measurements of positive ions during polar mesospheric winter echoes. *Atmos. Chem. Phys., 6*, 5515-5524.

Chau, J. L., et al. (2013), PMSE strength during enhanced D region electron densities: Faraday rotation and absorption effects at VHF frequencies, *Journal of Atmospheric and Solar-Terrestrial Physics*, http://dx.doi.org/10.1016/j.jastp.2013.06.015

Cho, J. Y. N., T. M. Hall, and M. C. Kelley (1992), On the role of charged aerosols in polar mesosphere summer echoes, *J. Geophys. Res.*, *97*, 875-886.

Cho, J. Y. N., and J. Röttger (1997), An updated review of polar mesosphere summer echoes: Observation, theory, and their relationship to noctilucent clouds and subvisible aerosols, *J. Geophys. Res.*, *102*, 2001-2020.

Czechowsky, P., R. Rüster, and G. Schmidt (1979), Variations of mesospheric structures in different seasons, *Geophys. Res. Lett.*, *6*, 459-462, doi:10.1029/GL006i006p00459.

Czechowsky, P., I. M.Reid, R. Rüster, and G.Schmidt (1989), VHF radar echoes observed in the summer and winter polar mesosphere over Andoya, Norway, *J. Geophys. Res.*, *94(D4)*, 5199-5217, doi:10.1029/JD094iD04p05199.

Driscoll, R.J., and L.A. Kennedy (1985), A model for the spectrum of passive scalars in an isotropic turbulence field, *Phys. Fluids*, *28*, 72-80.

Ecklund, W. L., and B. B. Balsley (1981), Long-term observations of the Arctic mesosphere with the MST radar at Poker Flat, Alaska, *J. Geophys. Res.*, *6*, 7775-7780, doi:10.1029/JA086iA09p07775.

Friedrich, M., M. Rapp, T. Blix, U.-P. Hoppe, K. Torkar, S. Robertson, S. Dickson, and K. Lynch (2012), Electron loss and meteoric dust in the mesosphere, *Ann. Geophys.*, *30*, 1495-1501, doi:10.5194/angeo-30-1495-2012.

Gregory, J. B., and A. H. Manson (1967), Mesospheric electron number densities at 35°S latitude, *J. Geophys. Res.*, *72(3)*, 1073-1080, doi:10.1029/JZ072i003p01073.

Hall, C. M., A. H. Manson, C. E. Meek, and S. Nozawa (2006), Isolated lower mesospheric echoes seen by medium frequency radar at 70° N, 19° E, *Atmos. Chem. Phys.*, *6*, 5307-5314, doi:10.5194/acp-6-5307-2006.

Havnes, O., and M. Kassa (2009), On the sizes and observable effects of dust particles in polar mesospheric winter echoes, *J. Geophys. Res.*, *114*, D09209, doi:10.1029/2008JD011276.

Havnes, O., C. La Hoz, M. T. Rietveld, M. Kassa, G. Baroni, and A. Biebricher (2011), Dust charging and density conditions deduced from observations of PMWE modulated by artificial electron heating, *J. Geophys. Res.*, *116*, D24203, doi:10.1029/2011JD016411.

Hedin, A. E. (1991), Extension of the MSIS Thermosphere Model into the middle and lower atmosphere, *J. Geophys. Res.*, *96(A2)*, 1159-1172, doi:10.1029/90JA02125.

Hunten, D. M., R. P. Turco, and O. B. Toon (1980), Smoke and dust particles of meteoric origin in the mesosphere and stratosphere, *J. Atmos. Sci.*, *37*, 1342-1357, doi:10.1175/1520-0469(1980)037<1342:SADPOM>2.0.CO;2

Kavanagh, A. J., F. Honary, M. T. Rietveld, and A. Senior (2006), First observations of the artificial modulation of polar mesosphere winter echoes, *Geophys. Res. Lett*., *33*, L19801, doi:10.1029/2006GL027565.

Kelley, M. C., D. T. Farley, J. Röttger (1987), The effect of cluster ions on anomalous VHF back-scatter from the summer mesosphere, *Geophys. Res. Lett*., *14*, 1031-1034.

Kero, A., J. Vierinen, C.-F. Enell, I. Virtanen, and E. Turunen (2008), New incoherent scatter diagnostic methods for the heated D-region ionosphere, *Ann. Geophys.*, *26*, 2273-2279.

Kirkwood, S. (2007), Polar mesosphere winter echoes: A review of recent results, *Adv. Space Res.*, *40*, 751-757, doi:10.1016/j.asr.2007.01.024.

Kirkwood, S., Barabash, V., Belova, E., Nilsson, H., Rao, T.N., Stebel, K., Osepian, A., Chilson, P.B. (2002), Polar mesosphere winter echoes during solar proton events, *Adv. in Polar Upper Atmos. Res.*, *16*, 111-125.

Kirkwood, S., E. Belova, U. Blum, C. Croskey, P. Dalin, K. - H. Fricke, R. A. Goldberg, J. Manninen, J. D. Mitchell, and F. Schmidlin (2006a), Polar mesosphere winter echoes during MaCWAVE, *Ann. Geophys.*, *24*, 1245-1255, doi:10.5194/angeo-24-1245-2006.

Kirkwood, S., P. Chilson, E. Belova, P. Dalin, I. Häggström, M. Rietveld, and W. Singer (2006b), Infrasound: The cause of polar mesosphere winter echoes?, *Ann. Geophys.*, *24*, 475-491, doi:10.5194/angeo-24-475-2006.

Kirkwood, S., A. Osepian, E. Belova, and Y.-S. Lee (2015), High-speed solar wind streams and polar mesosphere winter echoes at Troll, Antarctica, *Ann. Geophys.*, *33*, 609-622, doi:10.5194/angeo-33-609-2015.

Krishnaswamy, S., D. L. Detrick, and T. J. Rosenberg (1985), The inflection point method of determining riometer quiet day curves, *Radio Sci*., *20(1)*, 123-136, doi:10.1029/RS020i001p00123.

Kubo, K., T. Sugiyama, T. Nakamura, and S. Fukao (1997), Seasonal and interannual variability of mesospheric echoes observed with the middle and upper atmosphere radar during 1986-1995, *Geophys. Res. Lett.*, *24*, 1211-1214.

Latteck, R., and I. Strelnikova (2015), Extended observations of polar mesosphere winter echoes over Andøya (69°N) using MAARSY, *J. Geophys. Res. Atmos.*, *120*, 8216-8226, doi:10.1002/2015JD023291.

Lehmacher, G. A., E. Kudeki, A. Akgiray, L. Guo, P. Reyes, and J. Chau (2009), Radar cross sections for mesospheric echoes at Jicamarca, *Ann. Geophys.*, *27(7)*, 2675-2684, doi:10.5194/angeo-27-2675-2009.

Lübken, F.-J., B. Strelnikov, M. Rapp, W. Singer, R. Latteck, A. Brattli, U. - P. Hoppe, and M. Friedrich (2006), The thermal and dynamical state of the atmosphere during polar mesosphere winter echoes, *Atmos. Chem. Phys.*, *6*, 13-24, doi:10.5194/acp-6-13-2006.

Lübken, F.-J., W. Singer, R. Latteck, and I. Strelnikova (2007), Radar measurements of turbulence, electron densities, and absolute reflectivities during polar mesosphere winter echoes (PMWE), *Adv. Space Res.*, *40*, 758-764.

Lübken, F.-J. (2014), Turbulent scattering for radars: A summary, *J. Atmos. Sol. Terr. Phys., 107*, 1-7.

Makarevitch, R. A., and F. Honary (2005), Correlation between cosmic noise absorption and VHF coherent echo intensity, *Ann. Geophys.*, *23*, 1543-1553, SRef-ID: 1432-0576/ag/2005-23-1543.

McKinnell, L.-A., and M. Friedrich (2007), A neural network-based ionospheric model for the auroral zone, *J. Atmos. Sol. Terr. Phys., 69*, 1459-1470, doi:10.1016/j.jastp.2007.05.003.

Megner, L., D. E. Siskind, M. Rapp, and J. Gumbel (2008), Global and temporal distribution of meteoric smoke: A two-dimensional simulation study, *J. Geophys. Res.*, *113*, D03202, doi:10.1029/2007JD009054.

Morris, R. J., M. B. Terkildsen, D. A. Holdsworth, and M. R. Hyde (2005), Is there a causal relationship between cosmic noise absorption and PMSE?, *Geophys. Res. Lett.*, *32*, L24809, doi:10.1029/2005GL024568.

Nishiyama, T., K. Sato, T. Nakamura, M. Tsutsumi, T. Sato, M. Kohma, K. Nishimura, Y. Tomikawa, M. K. Ejiri, and T. T. Tsuda (2015), Height and time characteristics of seasonal and diurnal variations in PMWE based on 1 year observations by the PANSY radar (69.0°S, 39.6°E), *Geophys. Res. Lett.*, *42*, 2100-2108, doi:10.1002/2015GL063349.

Rapp, M., J. Gumbel, F.-J. Lübken, and R. Latteck (2002), D-region electron number density limits for the existence of polar mesosphere summer echoes, *J. Geophys. Res.*, *107* (D14), doi:10.1029/2001JD001323.

Rapp, M., and F.-J. Lübken (2004), Polar mesosphere summer echoes (PMSE): Review of observations and current understanding, *Atmos. Chem. Phys.*, *4*, 2601-2633.

Rapp, M., R. Latteck, G. Stober, P. Hoffmann, W. Singer, and M. Zecha (2011), First three-dimensional observations of polar mesosphere winter echoes: Resolving space-time ambiguity, *J. Geophys. Res.*, *116*, A11307, doi:10.1029/2011JA016858 .

Rosinski, J., and R. H. Snow (1961), Secondary Particulate Matter from Meteor Vapors., *J. Atmos. Sci.*, *18*, 736-745.

Sato, K., M. Tsutsumi, T. Sato, T. Nakamura, A. Saito, Y. Tomikawa, K. Nishimura, M. Kohma, H. Yamagishi, T. Yamanouchi (2014), Program of the Antarctic Syowa MST/IS radar (PANSY), *J. Atmos. Sol.-Terr. Phys.*, doi:10.1016/j.jastp.2013.08.022.

Sato, K., M. Kohma, M. Tsutsumi, and T. Sato (2017), Frequency spectra and vertical profiles of wind fluctuations in the summer Antarctic mesosphere revealed by MST radar observations, *J. Geophys. Res. Atmos.*, *122*, 3-19, doi:10.1002/2016JD025834.

Sato, T., A. Ito, W. L. Oliver, S. Fukao, T. Tsuda, S. Kato, and I. Kimura (1989), Ionospheric incoherent scatter measurements with the middle and upper atmosphere radar: Techniques and capability, *Radio Sci.*, *24(1)*, 85-98, doi:10.1029/RS024i001p00085.

Selvaraj, D., A. Patra, H. Chandra, H. Sinha, and U. Das (2014), Scattering cross section of mesospheric echoes and turbulence parameters from Gadanki radar observations, *J. Atmos. Sol. Terr. Phys.*, *119*, 162-172, doi:10.1016/j.jastp.2014.08.004.

Strelnikova, I., and M. Rapp (2013), Statistical characteristics of PMWE observations by the EISCAT VHF radar, *Ann. Geophys.*, *31*, 359-375, doi:10.5194/angeo-31-359-2013.

Tsuda, T., Y. Murayama, M. Yamamoto, S. Kato and S. Fukao (1990), Seasonal variation of momentum flux in the mesosphere observed with the MU radar, *Geophys. Res. Lett.*, *17*, 725-728, doi:10.1029/GL017i006p00725

Tsutsumi, M., and T. Aso (2005), MF radar observations of meteors and meteor-derived winds at Syowa (69°S, 39°E), Antarctica: A comparison with simultaneous spaced antenna winds, *J. Geophys. Res.*, *110*, D24111, doi:10.1029/2005JD005849.

Turunen, E., P. T. Verronen, A. Seppälä, C. J. Rodger, M. A. Clilverd, J. Tamminen, C.-F. Enell, and T. Ulich (2009), Impact of different energies of precipitating particles on NOx generation in the middle and upper atmosphere during geomagnetic storms, *J. Atmos. Sol. Terr. Phys., 71*, 1176-1189.

Zeller, O., M. Zecha, J. Bremer, R. Latteck, and W. Singer (2006), Mean characteristics of mesosphere winter echoes at mid- and high-latitudes, *J. Atmos. Sol. Terr. Phys.*, *68*, 1087-1104, doi:10.1016/j.jastp.2006.02.015.

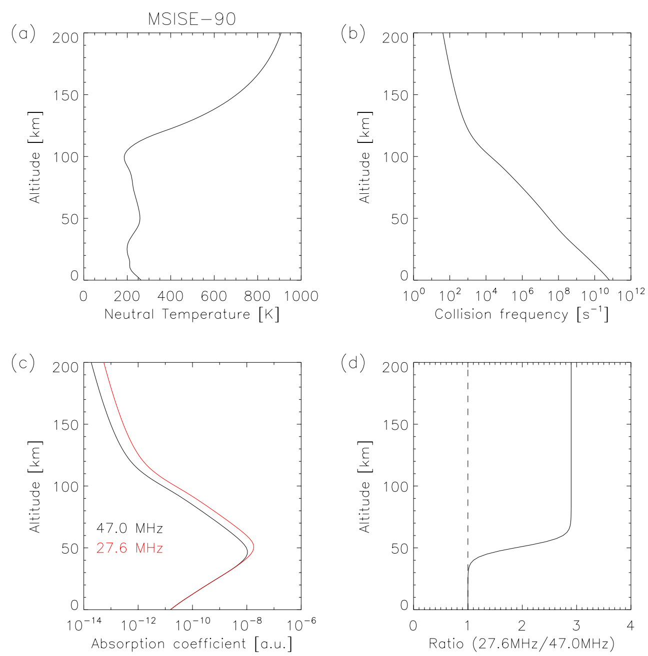

Figure A1. (a) Neutral temperature profile calculated by MSISE-90 [*Hedin*, 1991]; (b) Collision frequency between neutrals and electrons based on *Gregory and Manson* [1967]; (c) Absorption coefficient for 47.0 MHz (black) and 27.6 MHz (red) in arbitrary units; (d) Ratio of absorption coefficients at the two different frequencies. Note that above 60 km, the ratio remains constant with altitude.

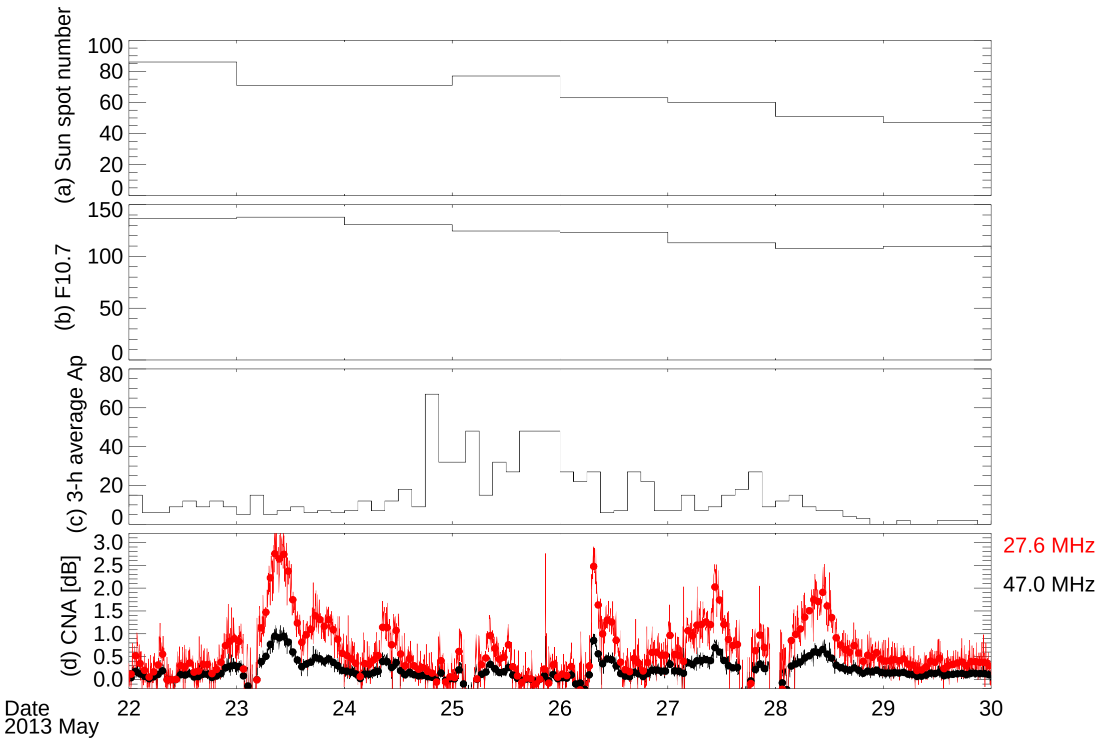

Figure A2. Overview of time variations in input parameters for IMAZ from 22 May to 29 May. Figure A2a and b are daily variations in sun spot number and in *F10.7* index, respectively. The third panel is temporal variations in the 3-hour averaged *Ap* index. The bottom panel shows temporal variations in CNA at the two frequencies. Black and red lines are the initially estimated 47.0 MHz CNA and the corresponding 27.6 MHz CNA, respectively. Small dots plotted on the lines indicate 1-hour averaged CNA.

Table 1. Basic radar parameter of the PANSY radar in May 2013[a]

Parameter	
Operational frequency	47 MHz
Antenna aperture	3900 m^2
Peak transmitting power	113 kW
# of antenna	228
# of multi-channel system	12
Inter pulse period	800 μs
# of coherent integration	16
# of incoherent integration	10
Polarization	circular-polarized waves

[a]Note that the PANSY radar was operating in a quarter system at that time.

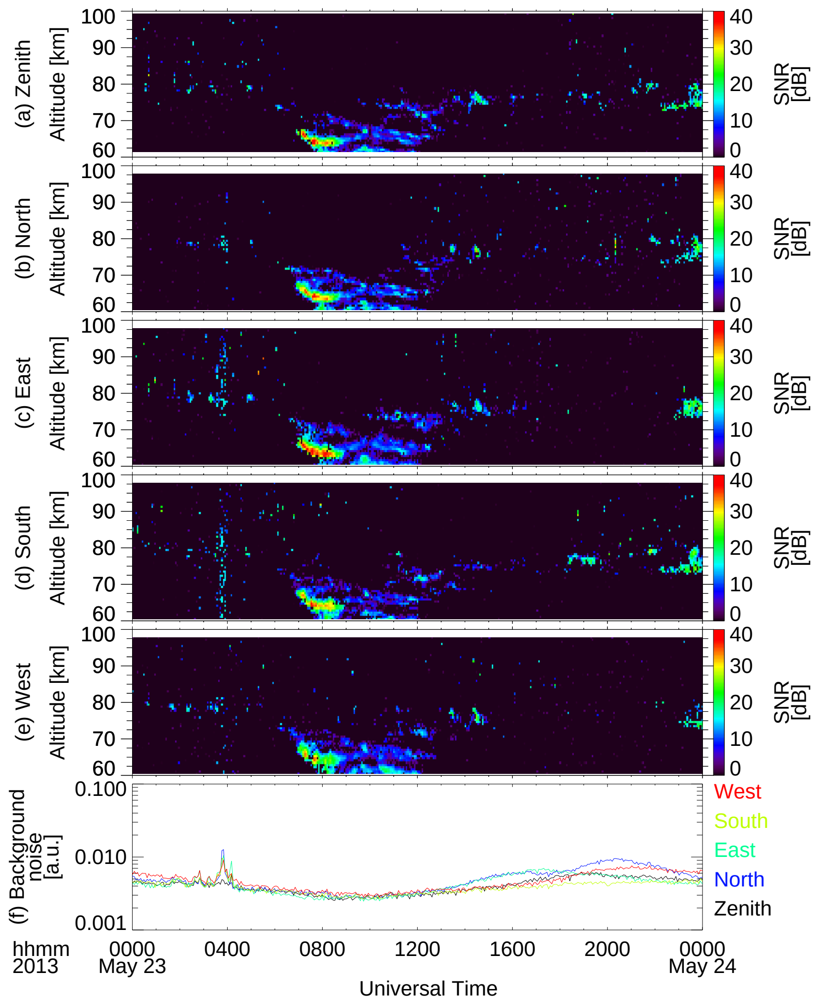

Figure 1. Height-time sections of backscattered echo power (SNR) and temporal variation in background noise measured by the PANSY radar on 23 May 2013. (a-e) Diurnal PMWE variations for five beams in different directions corresponding to local zenith, geographical north, east, south, and west. (f) Temporal variations in the noise due to cosmic noise power (CNP) as a function of time. The five different colors correspond to the five beams in the different directions. Note that the temporal variations in the noise in the each direction have already been subtracted from the backscattered echo power in the panels (a-e).

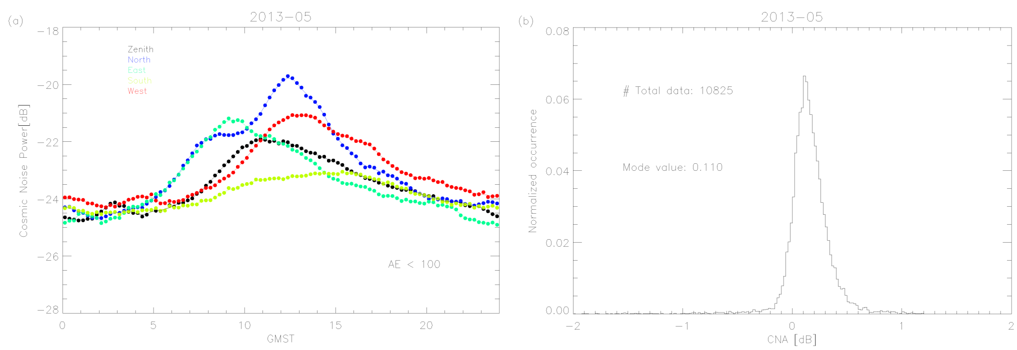

591 **Figure 2.** (a) Quiet day curve (QDC) as a function of GMST estimated by our analysis method. (b) Histogram of the obtained CNA in all five directions in May 2013.

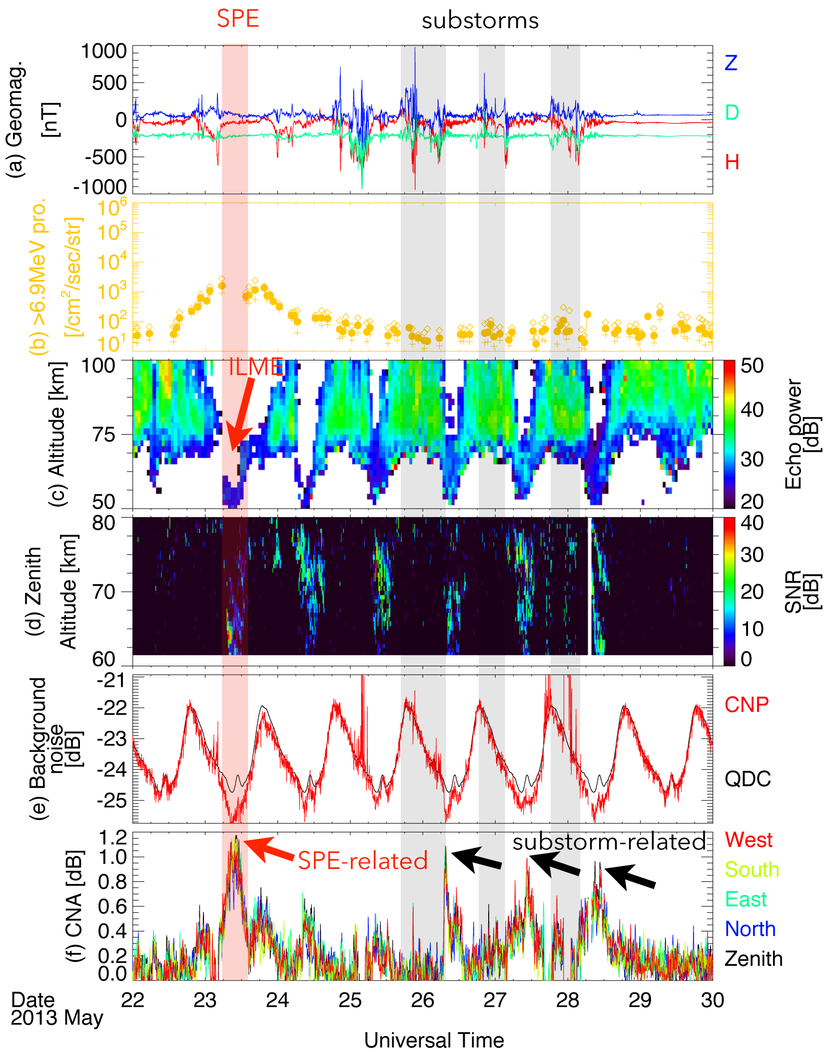

Figure 3. Overview of magnetospheric-ionospheric disturbances associated with the 23 May SPE and subsequent substorms from 22 May to 29 May. (a) Geomagnetic field variations observed at the Syowa station. Red, green, and blue lines indicate H, D, and Z components, respectively. (b) Field-aligned energetic proton flux (> 6.9 MeV) measured by NOAA/Polar Orbiting Environmental Satellites in the vicinity of Syowa. (c) and (d) Height and time sections of backscattered echo power observed by MF radar and the PANSY radar, respectively. (e) Black and red lines indicate temporal variations in QDC and CNP in the zenith direction, respectively. The many spikes seen in CNP are caused by interference. (f) CNA along the five beam directions. Note that the plots are running-averaged variations for about 12 minutes. Red and black arrows indicate peaks of SPE-related CNA and substorm-related CNA, respectively. Intervals of SPE and subsequent substorms are highlighted in semi-transparent red and gray. Note that the substorm-related CNA took place on the dayside and is likely due to EPP just after the substorms.

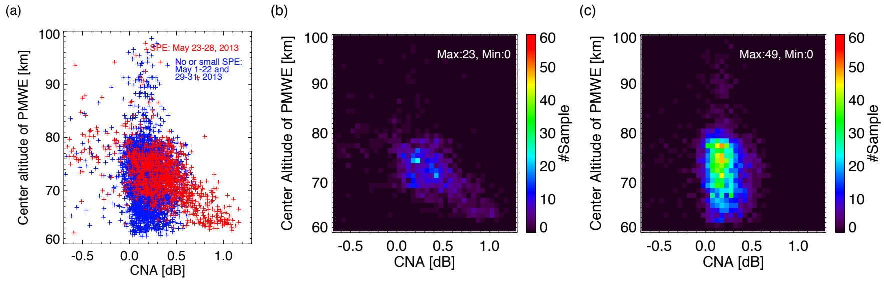

Figure 4. (a) Scatter plot of CNA and weighted mean center altitude (WMCA) of PMWE. Red and blue crosses represent data sampled during the disturbed period related to SPE and quiet period, respectively. (b) and (c) Two-dimensional data number distributions for CNA and the WMCA of PMWE during the disturbed period and the quiet period. Horizontal and vertical bin widths are 0.05 dB and 1.0 km, respectively.

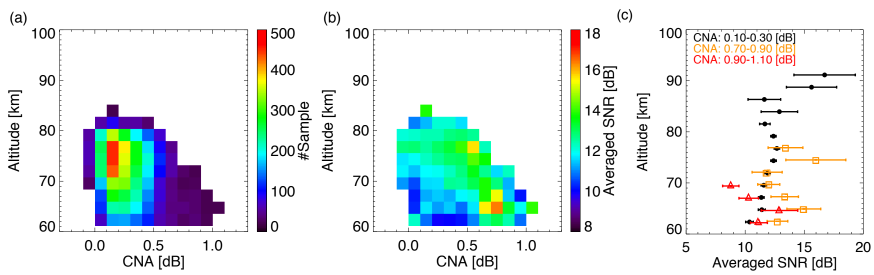

Figure 5. (a) and (b) Number and averaged SNR distributions for CNA and altitude. Horizontal and vertical bin widths are 0.1 dB and 2.4 km, respectively. (c) Averaged echo power profiles and their dependence on CNA magnitude. Error bars plotted with the profiles indicate 90% confidence intervals.

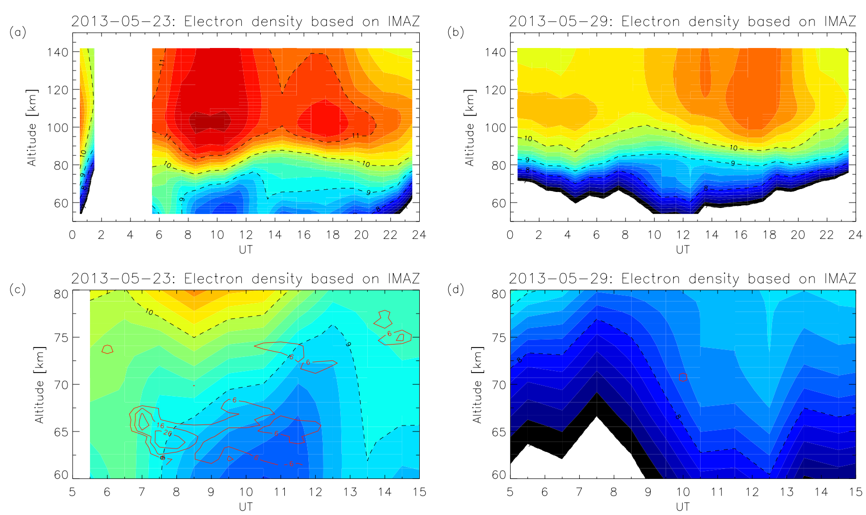

Figure 6. (a) and (b) Diurnal variations of electron density calculated by IMAZ during SPE and quiet periods, respectively. Dashed contour lines indicate electron density of 10^7, 10^8, 10^9, 10^{10}, and 10^{11} m^{-3}. The data gap in (a) is due to unreliable CNA estimates. (c) and (d) Expanded contour plots of the same data as in (a) and (b) between 05 and 15 UT and from 60 to 80 km. Red contour lines on the each electron density plot indicate PMWE SNR averaged for 30 minutes of 6, 16, and 26 dB.

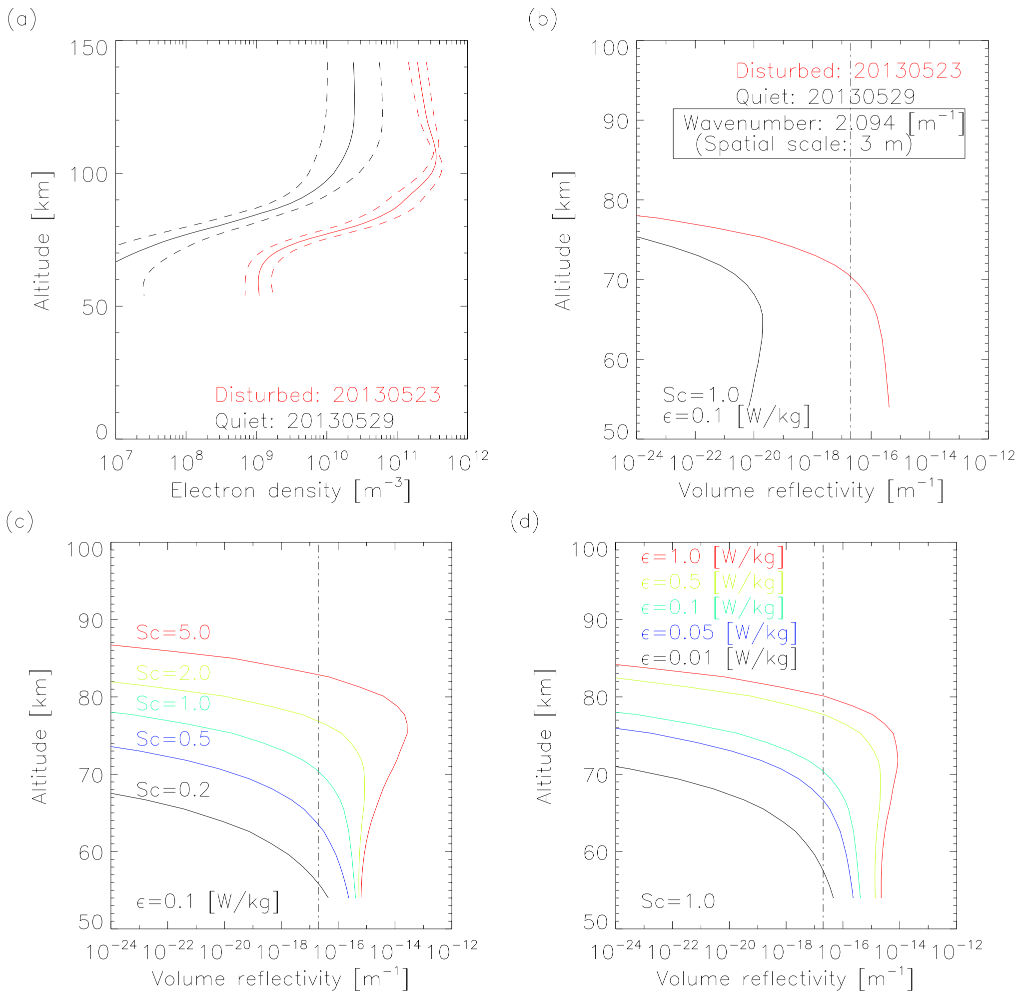

Figure 7. (a) Comparison of IMAZ electron density profiles at 0730 UT on 23 May (red) and on 29 May (black). Dashed lines indicate root mean square errors of electron density in the model. (b) Radar volume reflectivities as a function of altitude for coherent scattering from 3-m scale turbulent structures on the two dates. We used as input parameters kinematic viscosity (ν) deduced from MSISE-90, electron density (N_e) and vertical gradient of electron density (dN_e/dz) calculated from IMAZ. (c) and (d) Variability of radar volume reflectivities at 0730 UT on 23 May in the same format as (b) but with the five different Schmidt number (Sc) and turbulent energy dissipation rate (ε), respectively.